Synthesis, Structure, and Electric Conductivity of Ferrous Tainiolite and Its Oxidative Conversion into Coarse-Grained Swellable Smectite

Ruslan Mariychuk,[†] Alexander Baumgartner,[†] Friedrich E. Wagner,[‡] Anton Lerf,[§] Andreas Dubbe,[||] Ralf Moos,[||] and Josef Breu*,[†]

Lehrstuhl für Anorganische Chemie I and Lehrstuhl für Funktionsmaterialien, Universität Bayreuth, D-95440 Bayreuth, Germany, Physik-Department E15, Technische Universität München, D-85747 Garching, Germany, and Walther-Meissner-Institut, Bayerische Akademie der Wissenschaften, D-85748 Garching, Germany

Received May 21, 2007. Revised Manuscript Received August 2, 2007

Ferrous tainiolite, $Cs[Fe_2Li]^o[Si_4]^tO_{10}F_2$, has been synthesized from the melt in gastight molybdenum crucibles. The electric conductivity has been measured by impedance spectroscopy. As compared to natural micas, which are insulators, good conductivity is observed. The layered silicate can be further modified by ion exchange, which makes it a promising host structure for sensor materials. The estimated activation energy is as low as 0.79 eV. Upon Ba^{2+} exchange for Cs^+, structural Fe^{2+} is partially oxidized (33%), and the layer charge is reduced significantly, resulting in a coarse-grained but swollen (monolayer hydrate) smectite-type layered silicate. Therefore, further functionalization by pillaring will be feasible resulting in a conducting microporous material. The new material has been characterized by the analysis of chemical composition (wavelength dispersive X-ray spectroscopy and laser ablation-inductively coupled plasma−mass spectrometry), differential thermal analysis, electron microscopy, Mössbauer, UV−vis/NIR, impedance spectroscopy, and single-crystal structure refinement ($wR(F^2) = 0.0883$). The structure is of the 1*M* polytype (*C*2/*m*) with cell parameters $a = 5.277(2)$ Å, $b = 9.148(2)$ Å, $c = 10.804(2)$ Å, and $\beta = 99.19(3)°$. The congruent melting point was observed at 1103 (±5) K.

Introduction

The intercalation of large (metal-)organic or inorganic cations (pillars) into the interlayer space of layered silicates provides a flexible route to structures with a pseudo-two-dimensional system of micropores (pillared interlayer solids) with interesting properties, such as size and shape selectivity. In addition to the functionalization of the interlayer space, the silicate layer itself can also be engineered for desired physical properties such as magnetism or, particularly interesting, electric conductivity. A promising route to these properties is the incorporation of multivalent transition metals in concentrations far above natural levels in the silicate layer. The presence of transition metals in the silicate layer is not only essential for the desired physical properties but also enables one to alter the layer charge post-synthesis over a wide range by oxidizing the structural cations. This not only promotes the kinetics of incorporating pillars into the interlayer space but also allows for tailoring of the micropore size.

The combination of advantages of intercalation chemistry[1−3] (e.g., pseudo-two-dimensional structure, size selectivity, and shape selectivity) with functionalization of the silicate layer through transition metals (e.g., electric conductivity, magnetism, and adjustable layer charge) results in interesting microporous host systems that may be used for sensor materials or electrochemical devices.

Most commonly, naturally occurring swellable 2:1 clay minerals (smectites) are used as parent minerals for pillaring. Dehydrated natural smectites are insulators.[4,5] These natural smectites are nanosized materials and show a high degree of planar defects (turbostratic structures). This results in major difficulties in the interpretation of bulk analyses and X-ray diffraction patterns. Further complications follow from material-immanent accessory minerals. With hydrothermally synthesized smectites, none of the previously mentioned shortcomings can be overcome.[6−11]

* Corresponding author. Fax: (+49) 921-552788; e-mail: josef.breu@uni-bayreuth.de.
[†] Lehrstuhl für Anorganische Chemie I, Universität Bayreuth.
[‡] Technische Universität München.
[§] Bayerische Akademie der Wissenschaften.
[||] Lehrstuhl für Funktionsmaterialien, Universität Bayreuth.

(1) Behrens, M.; Kiebach, R.; Ophey, J.; Riemenschneider, O.; Bensch, W. *Chem.—Eur. J.* **2006**, *12*, 6348−6355.
(2) Behrens, M.; Riemenschneider, O.; Bensch, W.; Indris, S.; Wilkening, M.; Heitjans, P. *Chem. Mater.* **2006**, *18*, 1569−1576.
(3) Engelhard, M.; Grabner, E. W.; Bensch, W. *J. Electroanal. Chem.* **1996**, *415*, 79−84.
(4) Logsdon, S. D.; Laird, D. A. *Clays Clay Miner.* **2004**, *52*, 411−420.
(5) Haouzi, A.; Belarbi, H.; Giuntini, J. C.; Vanderschueren, J.; Staunton, S.; Zanchetta, J. V. *Clay Miner.* **2000**, *35*, 323−333.
(6) Carrado, K. A.; Thiyagarajan, P.; Song, K. *Clay Miner.* **1997**, *32*, 29−40.
(7) Vogels, R. J. M. J.; Breukelaar, J.; Kloprogge, J. T.; Jansen, J. B. H.; Geus, J. W. *Clays Clay Miner.* **1997**, *45*, 1−7.
(8) Iwasaki, T.; Onodera, Y.; Torii, K. *Clays Clay Miner.* **1989**, *37*, 248−257.
(9) Decarreau, A.; Colin, F.; Herbillon, A.; Manceau, A.; Nahon, D.; Paquet, H.; Trauthbadaud, D.; Trescases, J. J. *Clays Clay Miner.* **1987**, *35*, 1−10.
(10) Nakazawa, H.; Yamada, H.; Yoshioka, K. *Clay Sci.* **1991**, *8*, 59−68.

10.1021/cm0713778 CCC: $37.00
Published on Web 10/02/2007

Table 1. 2:1 Layered Silicates with High Contents of Transition Metals

formula	color
$K[Mn^{3+}{}_2Li]^o[Si_4]^tO_{10}(O)_2$[18]	
$K[Ni^{2+}{}_3]^o[AlSi_3]^tO_{10}(OH)_2$[19]	green
$K[Co^{2+}{}_3]^o[AlSi_3]^tO_{10}(OH)_2$[19]	violet
$K[Fe^{2+}{}_3]^o[AlSi_3]^tO_{10}(OH)_2$[19]	black
$K[Ni^{2+}{}_3]^o[Fe^{3+}Si_3]^tO_{10}(OH)_2$[20]	red−brown
$K[Co^{2+}{}_3]^o[Fe^{3+}Si_3]^tO_{10}(OH)_2$[20]	red−brown
$K[Fe^{2+}{}_3]^o[Fe^{3+}Si_3]^tO_{10}(OH)_2$[20]	black
$Cs[Fe^{2+}{}_3]^o[Fe^{3+}Si_3]^tO_{10}(OH)_2$[21]	gray
$K[Ni^{2+}{}_2Li]^o[Si_4]^tO_{10}F_2$[22]	green
$K[Co^{2+}{}_2Li]^o[Si_4]^tO_{10}F_2$[23]	pink

In contrast, there are many reports in the literature of both synthetic and natural micas that have contents of transition metals far above the natural abundance levels (Table 1). These mica materials are coarse-grained and are analytically and structurally well-characterized. Interestingly, despite the numerous research papers dedicated to micas, the knowledge about important physical properties such as electric conductivity is limited. Also, although cation exchange for micas is possible in principle,[12−16] concomitant ion exchange and redox reactions have not been investigated for these synthetic micas. This is even more astonishing since it has long been known that the presence of transition metals in micas supports transformation into vermiculites through oxidation and ion exchange.[17] For instance, the increase of the Fe^{3+}/Fe^{2+} ratio in the octahedral layer leads to the decrease of interlayer space occupation and the formation of interlayer vacancies. As a consequence, access to the interlayer space is enhanced, and vermiculites can be further functionalized through pillaring by large cations yielding size- and shape-selective microporous materials.

Synthetic transition-metal-free (fluoro-)micas have found widespread applications as good insulator materials due to their high electric resistance. Tate[24] et al. reported that the electric resistivity of fluoro-phlogopite $K[Mg_3]^o[AlSi_3]^tO_{10}F_2$ at 500 °C is as high as 10^{11} to 10^{12} Ω cm in the direction perpendicular to the silicate layers and 10^6 to 10^7 Ω cm parallel to the layers. The band gap for a synthetic hydroxo-mica $K[Mg_3]^o[AlSi_3]^tO_{10}(OH)_2$[25] is reported to be ≈7.7 eV.

To our knowledge, there are no electric conductivity measurements of synthetic fluoro-micas containing transition metals. However, a few reports about electric conductivity of natural micas with relatively high contents of iron (0.05−1.43 Fe^{2+} per formula unit) exist in the literature.[25−30] According to Guseinov et al.,[30] the incorporation of two Fe^{2+} per formula unit, as in $Cs[Fe_2Li]^o[Si_4]^tO_{10}F_2$, should increase the electric conductivity significantly by up to 5 orders of magnitude.

For that reason, this study deals with the search for conducting 2:1 layered silicates as promising hosts for sensor materials. The object of the current investigation is completely iron substituted tainiolite $Cs[Fe_2Li]^o[Si_4]^tO_{10}F_2$.

Experimental Procedures

The high purity reagents (in total, approximately 50 g) of CsF (Aldrich, 99.9%), LiF (Aldrich, 99.9%), SiO_2 (Merck, fine granular, calcined), and Fe_2SiO_4 were weighed in an Ar atmosphere according to the composition $Cs[Fe_2Li]^o[Si_4]^tO_{10}F_2$. Stoichiometric Fe_2SiO_4 has been produced by melt synthesis from Fe_2O_3 (Aldrich, 99.9%) and SiO_2 (Merck, fine granular, calcined) in a 1:1 ratio followed by annealing in quartz tubes at a fixed oxygen partial pressure to ensure the Fe^{2+} valence state ($CO/CO_2 = 1$ and $T = 1403$ K). Phase purity of synthesized Fe_2SiO_4 has been checked by X-ray diffraction analysis and Mössbauer spectroscopy, and it was ocher.

The melt synthesis of the final product was performed in sealed molybdenum crucibles according to a procedure described previously.[31] The molybdenum crucibles (25 mm outer diameter, 21 mm inner diameter, and 180 mm overall length) were manufactured by drilling from a rod of pure molybdenum (Plansee). After being loaded with the reagents, the crucible was closed with a fitting lid and was then sealed in a radio frequency induction furnace by application of short radiation pulses of less than 40 s. To protect the crucible from oxidation at high temperatures, it was placed in a quartz tube under vacuum ($<10^{-4}$ Torr). The sealed crucible was then heated in a graphite furnace (Graphit HT-1900, Linn High Therm) for the actual synthesis. To minimize gravity segregation in the melt, the crucible was positioned horizontally in the furnace and rotated with 60 rpm during the synthesis. The synthesis was carried out at a maximum temperature of 2020 K for 1 h, followed by slow cooling to 1070 K at a rate of 3 K/min. Finally, the crucible was quenched by switching off the power supply.

The melting point of the synthesized product was determined by differential thermal analysis (DTA) using a Linseis L81 thermoanalyzer. Heating/cooling cycles were performed in sealed molybdenum crucibles containing about 100 mg of the sample in the temperature range of 323−1523 K at a rate of 10 K/min in an Ar atmosphere. An empty molybdenum crucible was used as the reference.

The chemical composition of the sample was determined by wavelength dispersive X-ray spectroscopy (WDX) using an electron microprobe (Jeol JXA-8200, Bayerisches Geoinstitut, Bayreuth) operated at the following settings: acceleration voltage 15 kV, initial

(11) Yamada, H.; Yoshioka, K.; Nakazava, H. *Mineral. J.* **1991**, *15*, 300−308.
(12) Keppler, H. *Am. Mineral.* **1990**, *75*, 529−538.
(13) Ross, G. J.; Rich, C. I. *Clays Clay Miner.* **1973**, *21*, 77−81.
(14) Bracke, G.; Satir, M.; Krauss, P. *Clays Clay Miner.* **1995**, *43*, 732−737.
(15) von Reichenbach, H.; Rich, C. I. *Clays Clay Miner.* **1969**, *17*, 23−29.
(16) von Reichenbach, H. In *Proceedings of the International Clay Conference in Madrid*, 1972; Serratosa, J. M., Eds.; J. M. Division de Ciencias, CSIC: Madrid, 1973; p 457.
(17) Vicente, M. A.; Razzaghe, M.; Robert, M. *Clay Miner.* **1977**, *12*, 101−112.
(18) Gnos, E.; Armbruster, T.; Villa, I. M. *Am. Mineral.* **2003**, *88*, 189−194.
(19) Redhammer, G. J.; Amthauer, G.; Lottermoser, W.; Bernroider, M.; Tippelt, G.; Roth, G. *Miner. Petrol.* **2005**, *85*, 89−115.
(20) Hazen, R. M.; Wones, D. R. *Am. Mineral.* **1972**, *57*, 103−129.
(21) Comodi, P.; Zanazzi, P. F.; Weiss, Z.; Rieder, M.; Drabek, M. *Am. Mineral.* **1999**, *84*, 325−332.
(22) Kitajima, K.; Ihara, Y.; Takusagawa, N. *J. Ceram. Soc. Jpn.* **1995**, *103*, 1057−1062.
(23) Ihara, Y.; Kitajima, K. *J. Ceram. Soc. Jpn.* **1997**, *105*, 881−885.
(24) Tate, I.; Kitajima, K.; Daimon, N.; *Kogyo Kagaku Zasshi* **1968**, *71*, 976−980.
(25) Davidson, A. T.; Yoffe, A. D. *Phys. Status Solidi* **1968**, *30*, 741−754.
(26) Crine, J. P.; Friedmann, A.; Wertheimer, M. R.; Yelon, A. *Can. J. Phys.* **1977**, *55*, 270−275.
(27) Meunier, M.; Currie, J. F.; Wertheimer, M. R.; Yelon, A. *J. Appl. Phys.* **1983**, *54*, 898−905.
(28) Tolland, H. G.; Strens, G. J. *Phys. Earth Planet. Inter.* **1972**, *5*, 380−386.
(29) Guseinov, A. A. *Fiz. Zemli* **1999**, 75−82.
(30) Guseinov, A. A.; Gargatsev, I. O.; Gabitova, R. U. *Izv. Phys. Solid Earth* **2005**, *41*, 670−679.
(31) Breu, J.; Seidl, W.; Stoll, A. J.; Lange, K. G.; Probst, T. *Chem. Mater.* **2001**, *13*, 4213−4220.

Table 2. Crystallographic Data and Details of Structure Determination of $Cs[Fe_2Li]^o[Si_4]^tO_{10}F_2$

Crystal Data	
$Cs_{0.986(6)}[Fe_{2.03(3)}Li_{0.97(4)}]^o[Si_4]^tO_{10}F_2$	
$M_r = 561.586$	monoclinic, *C*2/*m* (No. 12)
Mo Kα radiation	cell parameters from 5900 reflections ($\theta = 2.3-30.0°$)
$T = 293$ K	$Z = 2$
$a = 5.277(2)$ Å	$\mu = 6.834$ mm^{-1}
$b = 9.148(2)$ Å	plate, brown
$c = 10.804(2)$ Å	0.29 mm × 0.27 mm × 0.02 mm
$\beta = 99.19(3)°$	$D_x = 3.621$ Mg m^{-3}
$V = 514.9(2)$ Å^3	
Data Collection	
STOE IPDS I diffractometer, rotation scans 2576 recorded, 766 independent reflections, *735 reflections with* $I > 2\sigma(I)$	
absorption correction: numerical via equivalents,[34] $T_{min} = 0.3777$ and $T_{max} = 0.9161$	
$R_{int} = 0.0497$	$h = -7 \rightarrow 7$
$\theta_{max} = 30.02$	$k = -12 \rightarrow 12$
	$l = -15 \rightarrow 15$
Refinement	
refinement on F^2	
$R(F) = 0.0365$	$\Delta\rho_{max} = 1.642$
$wR(F^2) = 0.0883$	$\Delta\rho_{min} = -0.752$
$S = 1.108$	$(\Delta/\sigma)_{max} = 0.000$
766 reflections	58 parameters
$w = 1/[\sigma^2(F_o^2) + (0.0389P)^2 + 4.5755P]$ where $P = (F_o^2 + 2F_c^2)/3$	

beam current 15 nA, and beam spot diameter 1 μm. Magnesium oxide (O), andradite (Si), pure iron (Fe), fluorite (F), and pollucite (Cs) were used as standards. The counting time was 20 s at the peak position and 10 s on each side of the peak position. The mica sample was embedded in resin on a glass slide, polished to a flat surface, and coated with carbon. Because of the inability of this method to determine the Li content, the composition of the layered silicate was normalized to $Si_{4.00}$ and then further normalized to 22 negative charges to calculate the Li content of the sample. The esd values for the composition were calculated with the same normalization method based on the error values received from the measurements.

Additionally, the amount of lithium was verified by laser ablation-inductively coupled plasma-mass spectrometry (LA-ICP−MS). The utilized LA-ICP−MS system consisted of an Elan DRC-e quadrupole mass spectrometer (PerkinElmer Instruments) attached to a Geolas M 193 nm ArF Excimer Laser system (Coherent/Lambda Physik). Technical details about this system can be found in the literature.[32] Samples were pressed to pellets without any additives. Ablation was performed using laser beam sizes ranging from 5 to 20 μm in diameter. The laser was operated at a frequency of 10 Hz and a power of 25 kV. The sample chamber was flushed with helium gas at a rate of 1 L/min, to which Ar was added on the way to the ICP−MS. Signals were recorded with 5 sweeps per second, and the instrument background was measured for 30 s before each analysis. Integrated signal intensities were referenced to NIST SRM 610 glass according to routines described elsewhere.[33] Element ratios were turned into stoichiometric coefficients by normalization to $Si_{4.00}$.

For the X-ray data collection, a carefully examined single crystal with a dimension of 0.29 mm × 0.27 mm × 0.02 mm was selected, which was free from diffuse streaks due to stacking disorder. The intensity data were collected at 293 K on a STOE IPDS I diffractometer using graphite-monochromated Mo Kα radiation. A numerical absorption correction was applied using the program X-RED[34] based on a crystal description optimized using equivalent reflections with X-SHAPE.[34] Starting with atomic coordinates taken from $Cs_{0.6}[Mg_{2.4}Li_{0.6}]^o[Si_4]^tO_{10}F_2$,[35] the refinement on F^2 was carried out using SHELXL97.[36] During refinement, the 4*h* and 2*d* positions were assumed to be fully occupied by a mixture of Fe^{2+} and Li^+. The occupancy of the interlayer position was refined without constraints. All atoms were refined with anisotropic displacement parameters. Crystal data and further details of the data collection are given in Table 2.

^{57}Fe Mössbauer spectra of powdered samples were measured at 298 and 170 K with a source of ^{57}Co in a rhodium matrix kept at ambient temperature and using α-Fe for velocity calibration. The spectra were least-squares fitted with line shapes corresponding to a Gaussian broadening of Lorentzian lines (Voigt profiles) grouped into quadrupole doublets.

A Cary 5 UV−vis/NIR spectrometer (Varian Techtron Pty.) was employed for the investigation of the reflectance spectrum, which was transformed into an absorption spectrum through the Kubelka−Munk function $\alpha/S = (1 - R)^2/2R$ (α is the absorption coefficient, *R* is the reflectance at a given wavelength, and *S* is the scattering coefficient).[37] $BaSO_4$ powder was used as the white standard.

For the impedance measurements, two plane-parallel polished discs (diameter 6.4 mm and thicknesses 1.05 and 1.65 mm) were ground from the as-prepared sample material. The surfaces were sputter-coated with 15 nm gold and were contacted by spring-loading with gold sheets in an alumina sample holder. The impedance was measured at frequencies between 10^{-2} and 10^7 Hz at 333−523 K (Novocontrol Alpha Analyzer, 0.15 V amplitude) in a tube furnace continuously purged with 10% O_2 in N_2 (99.999%).

For ion exchange, the layered silicate $Cs[Fe_2Li]^o[Si_4]^tO_{10}F_2$ obtained by melt synthesis was ground (Fritsch Pulverizette 14) and sieved to a particle size smaller than 125 μm. A suspension of 500 mg (approximately 0.9 mmol) of $Cs[Fe_2Li]^o[Si_4]^tO_{10}F_2$ in 50 mL of a saturated $Ba(ClO_4)_2$ solution (approximately 5.9 mol/L of

(32) Günther, D.; Frischknecht, R.; Heinrich, C. A.; Kahlert, H. J. *J. Anal. Atom. Spectrom.* **1997**, *12*, 939−944.
(33) Longerich, H. P.; Jackson, S. E.; Günther, D. *J. Anal. Atom. Spectrom.* **1996**, *11*, 899−904.
(34) *X-SHAPE* and *X-RED*; Stoe and Cie; Darmstadt, Germany, 1996.
(35) Breu, J.; Seidl, W.; Stoll, A. J. *Z. Anorg. Allg. Chem.* **2003**, *629*, 503−515.
(36) Sheldrick, G. M. *SHELXS97* and *SHELXL97*; University of Göttingen: Göttingen, Germany, 1997.
(37) Kubelka, P.; Munk, F. *Z. Tekh. Fiz.* **1931**, 593−597.

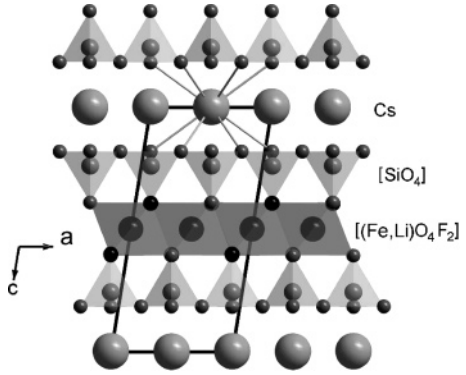

Figure 1. Polyhedral representation of the structure of $Cs[Fe_2Li]^o[Si_4]^tO_{10}F_2$ in the projection along *b* showing the 2:1 layer and its interconnection by the interlayer cations.

Ba^{2+}) was heated under reflux for 24 h. The procedure was repeated 6 times. Ba^{2+} was chosen as the exchanging cation because of its high selectivity for the interlayer space and because of its high hydratization energy, which leads to hydrated interlamellar spaces that foster further ion exchange.

The product of this ion exchange was characterized by powder X-ray diffraction (PXRD, Panalytical X'Pert Pro diffractometer in reflection mode, Cu Kα radiation, graphite secondary monochromator, and flat sample holder), LA-ICP−MS, and energy dispersive X-ray analysis (EDX, Jeol JSM 6300 equipped with a Ge detector). Since the exchange procedure was deliberately performed under air, Mössbauer measurements were carried out to determine the Fe^{3+}/Fe^{2+} ratio of the layered silicate.

Results and Discussion

The specimen obtained by the melt synthesis was an aggregate of transparent brown crystals with micaceous cleavage. The chemical compositions of the synthesized material as determined by WDX analysis ($Cs_{0.97(3)}[Fe_{2.03(6)}Li_{0.96(3)}]^o[Si_4]^tO_{10}F_2$, Li content calculated via charge neutrality), LA-ICP−MS ($Cs_{0.98(5)}[Fe_{1.93(10)}Li_{1.01(5)}]^o[Si_{4.00}]^tO_{10}F_2$), and single-crystal structure refinement ($Cs_{0.986(6)}[Fe_{2.03(3)}Li_{0.97(4)}]^o[Si_4]^tO_{10}F_2$) all are in close agreement to the ideal formula. DTA measurements yielded a congruent melting point of 1103 (±5) K.

Crystal Structure. The mica structure is well-known[38,39] and shall be discussed only briefly here. However, due to the large Fe^{2+} content, the size of the octahedral layer is large as compared to natural micas. The structural adjustments triggered by the large octahedral layer will therefore be discussed in some detail.

The polyhedral representation of the structure of $Cs[Fe_2Li]^o[Si_4]^tO_{10}F_2$ in the projection along *b* is shown in Figure 1. One octahedral layer $[(Fe,Li)O_4F_2]$ is surrounded by two tetrahedral layers $[SiO_4]$ and a layer of interlayer cations (Cs^+). In the tetrahedral layer, individual $[SiO_4]$ tetrahedra are linked with neighboring tetrahedra by sharing three corners each (basal oxygen atoms) to form an infinite two-dimensional hexagonal mesh pattern. The fourth oxygen atom (apical oxygen atom) forms one corner of the octahedral coordination unit around the (Fe,Li) cations. Thus, each octahedron consists of four apical oxygen atoms (two from the upper and two from the lower tetrahedral layer) and two F^- anions. The F^- sites are at the same height as the apical oxygen atoms but are not connected to the tetrahedral layer. Within the octahedral layer, individual octahedra are linked laterally by sharing edges. The smallest structural unit contains three octahedral sites. The negatively charged silicate layers are bound together by Cs^+ interlayer cations.

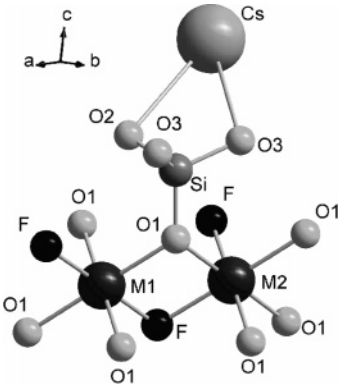

Figure 2. Part of the $Cs[Fe_2Li]^o[Si_4]^tO_{10}F_2$ structure.

Table 3. Atomic Coordinates of $Cs[Fe_2Li]^o[Si_4]^tO_{10}F_2$

atom	site	occupancy	*x/a*	*y/b*	*z/c*
Cs	2a	0.986(6)	0	0	0
M1	2d	0.749(9) Fe^{2+} 0.251(4) Li^+	1/2	0	1/2
M2	4h	0.638(7) Fe^{2+} 0.362(13) Li^+	0	0.1672(1)	1/2
Si	8j	1	0.0810(2)	0.3334(1)	0.2419(1)
O1	8j	1	0.1303(5)	0.3337(3)	0.3916(3)
O2	4i	1	−0.4389(7)	0	0.1823(4)
O3	8j	1	0.1894(5)	0.2501(3)	−0.1831(3)
F	4i	1	0.1306(6)	0	0.3958(3)

The octahedral layer of the trioctahedral mica contains two different octahedral sites, namely, the M1 (trans) and M2 (cis) sites (M1/M2 = 1:2), which differ by the configuration (cis or trans) of the two F^- (Figure 2). The final atomic parameters are given in Table 3. As expected, a slight preference of the relatively larger Fe^{2+} cations for the larger M1 position was observed by single-crystal refinement.

Usually, in natural micas, the lateral dimension of the octahedral layer is distinctly smaller than that of the tetrahedral layer. Different mechanisms for resolving this structural mismatch between the two building blocks interconnected by common oxygen atoms have been proposed.[20,40] Apart from bond length alteration (both in the octahedral and in the tetrahedral layer) and tilting/corrugation of the tetrahedral layer out of the (001) plane, the rotation of the tetrahedra perpendicular to the (001) plane and the flattening of the octahedral layer are regarded as the most effective mechanisms.

However, for the synthesized ferrous tainiolite, layer size calculations based on Shannon and Prewitt radii[41] show that

(38) Bailey, S. W. Crystal Chemistry of True Micas. *Micas*; Mineralogical Society of America: Chelsea, MI, 1984; pp 13−60.
(39) (a) Brigatti, M. F.; Guggenheim, S. Mica crystal chemistry and the influence of pressure, temperature, and solid solution on atomistic models. In *Micas: Crystal Chemistry and Metamorphic Petrology*; Mineralogical Society of America: Washington, DC, 2002; pp 1−97. (b) Liebau, F. *Structural Chemistry of Silicates*; Springer: Berlin, 1985; p 24.
(40) Donnay, G.; Donnay, J. D. H.; Takeda, H. *Acta Crystallogr.* **1964**, *17*, 1374−1381.
(41) Shannon, R. D.; Prewitt, C. T. *Acta Crystallogr., Sect. B: Struct. Sci.* **1969**, *B 25*, 925−946.

Table 4. Selected Geometric Parameters for $Cs[Fe_2Li]^o[Si_4]^tO_{10}F_2$

octahedral site		bond length (Å)
M1−O	×4	2.101(3)
M1−F	×2	2.089(4)
mean		2.098
M2−O	×2	2.104(3)
M2−O	×2	2.109(3)
M2−F	×2	2.080(3)
mean		2.098
tetrahedral site		**bond length (Å)**
Si−O1		1.597(3)
Si−O3		1.653(3)
Si−O3		1.643(3)
Si−O2		1.651(2)
mean		1.636
		angle (deg)
Si−O2−Si		134.8(1)
Si−O3−Si	×2	135.3(2)

the octahedral layer is actually considerably larger than the tetrahedral layer. Consequently, the coexistence of $[(Fe_2Li)O_4F_2]$ octahedral and $[SiO_4]$ tetrahedral layers as required for $Cs[Fe_2Li]^o[Si_4]^tO_{10}F_2$ composition is problematic. The calculated average lateral dimension of the octahedral layer (d_o) is 2.130 Å when the following bond lengths are used: Fe−O, 2.160 Å; Fe−F, 2.090 Å; Li−O, 2.140 Å; and Li−F, 2.070 Å. The lateral dimension of the tetrahedral layer (d_t) is estimated as 1.607 Å by using a regression equation by Brigatti and Guggenheim.[39a] These values give a ratio of $d_o/d_t = 1.299$, which is supposed to be impossible regarding geometrical considerations. Formally, the expected tetrahedral rotation angle would have to be negative ($\alpha \approx -7°$), which is of course impossible.

To solve this mismatch, the following adjustment mechanisms take effect to achieve the size matching of layers: the first is a significant bond length alteration (Table 4). The structural deformation is reflected in an unusually small difference between (Fe,Li)−O and (Fe,Li)−F bond lengths. The average bond lengths (2.098 Å) in the octahedral layer are smaller than estimated by Shannon and Prewitt radii (2.130 Å). The average size of both octahedra are similar, but it is important to note that similar average values do not mean that the bonding properties of the two types of octahedra are equal (as can be seen by the Mössbauer spectroscopy measurement).

The average bond length in the SiO_4 tetrahedron is longer (1.636 Å) than estimated (1.607 Å) when applying the equation given by Brigatti and Guggenheim.[39a] Another interesting point is the significant difference of the $Si-O1_{apical}$ and $Si-(O2,O3)_{basal}$ bond lengths. Probably, the asymmetrical displacement of the octahedral cations toward F^- produces a charge deficiency on the apical O atom, which is balanced by a short $Si-O_{apical}$ bond and an increased tetrahedral rotation angle (τ) (Table 5). As a consequence, only the $Si-O_{basal}$ bond lengths should be used to calculate the tetrahedral layer size. Somewhat surprisingly, the strain immanent in the structure is not reflected in the Si−O−Si bond angles (Table 4). According to Liebau's compilation, all angles are in the expected range.[39b]

The second adjustment mechanism is a reduction of the flattening of the octahedra along the *c* direction perpendicular to the planes. The octahedral flattening angle ψ (defined by $\sin \psi = b/3\sqrt{3}d_o$)[40] is smaller than usual, which results in an increase of the octahedral layer thickness as presented in Table 5 together with selected structure parameters for $Cs[Fe_2Li]^o[Si_4]^tO_{10}F_2$ and $Cs_{0.6}[Mg_{2.4}Li_{0.6}]^o[Si_4]^tO_{10}F_2$ but in a decrease of the lateral dimension (*ab*) of the layer (Table 4).

Table 5. Selected Structural Parameters of $R_x[M_{3-x}Li_x]^o[Si_4]^tO_{10}F_2$[a]

	$[Mg_{2.4}Li_{0.6}]$[35]	$[Fe_2Li]$
a (Å)	5.240(1)	5.277(2)
b (Å)	9.094(1)	9.148(2)
c (Å)	10.797(1)	10.804(2)
β (deg)	99.21(2)	99.19(3)
ab (Å^2)	47.65	48.27
α (deg)	0.74	0.20
τ (deg)	111.5	112.4
ψ_{M1} (deg)	58.41	57.07
ψ_{M2} (deg)	58.31	57.07
$\langle\psi\rangle$ (deg)	58.35	57.07
h_t (Å)	2.198(1)	2.226(3)
h_o (Å)	2.084(2)	2.311(3)
h_i (Å)	4.020(3)	3.904(2)

[a] α: tetrahedral rotation angle; τ: mean tetrahedral flattening angle; ψ_{M1}: octahedral flattening angle of M1; ψ_{M2}: octahedral flattening angle of M2; $\langle\psi\rangle$: av octahedral flattening angle; h_t: thickness of tetrahedral layer; h_o: thickness of octahedral layer; and h_i: interlayer separation.

For the composition given, one would actually expect a minimization of the size of the octahedral layer and hence an ideal octahedron ($\psi = 54.74°$). However, it should be noted that the flattening is caused not only by the mismatch but also by topological reasons. Shared O−O edges of a polyhedron are generally shorter than unshared edges, leading to a distortion within the layer of edge-sharing octahedra. The M−F bond length is generally shorter than M−O bond length, which also contributes to the distortion of the octahedra. Usual values for the octahedral flattening angles ψ for micas are in the range of 59−60°.[42] Redhammer et al.[19] have arrived at the conclusion that $\psi < 58.2°$ is impossible for the $[FeO_4(OH)_2]^o$ octahedron in micas. In $Cs[Fe_2Li]^o[Si_4]^tO_{10}F_2$, the octahedra have an average octahedral flattening angle of $\psi = 57.07°$. A further decrease of the octahedral flattening angle is limited by the previously mentioned topological reasons. But, lowering the octahedral flattening angle below the limit proposed by Redhammer et al.[19] is essential to decrease the size of the octahedral layer to match the tetrahedral layer.

The third adjustment mechanism is tetrahedral rotation. The tetrahedral rotation angle α ($\cos \alpha = b/4\sqrt{2}d_t$) is near zero (0.20°). Only the $Si-O_{basal}$ bond lengths are included into the calculation of α for the previously mentioned reasons. The rotation of tetrahedra would result in a decrease of the lateral dimension of the tetrahedral layer.[38] This is why a negative correlation between the average size of octahedra and the tetrahedral rotation angle is observed. As the tetrahedral layer in $Cs[Fe_2Li]^o[Si_4]^tO_{10}F_2$ is too small, we can expect $\alpha = 0°$. However, the actual value is slightly larger than zero. This could be associated with the thermal expansion since the compound crystallized at a temperature much higher than the temperature of the structure determination.

(42) Weiss, Z.; Rieder, M.; Chmielova, M.; Krajicek, J. *Am. Mineral.* **1985**, *70*, 747−757.

Table 6. Bulk Compositions As Determined by LA-ICP−MS before and after Oxidative Cation Exchange

Cs-tainiolite	$Cs_{0.98(5)}[Fe_{1.93(10)}Li_{1.01(5)}]^o[Si_{4.00}]^tO_{10}F_2$
Ba-smectite	$Ba_{0.23(1)}Cs_{0.10(1)}[Fe_{1.84(9)}Li_{0.68(3)}]^o[Si_{4.00}]^tO_{10}F_2$

Summarizing, the incorporation of relatively large Fe^{2+} cations into the octahedral layer can be achieved mainly by an increase of the *a* and *b* cell parameters and an increase in the height of the octahedral layer (h_o) (Table 5). The height of the tetrahedral layer (h_t) also increases due to an enlargement of the tetrahedra, while the interlayer separation (h_i) decreases due to the enlargement of the hexagonal cavities formed by the basal surfaces of the tetrahedra. No noticeable change in the *c* cell parameter is observed because the increase in the thickness of the octahedral and tetrahedral layers is compensated by the decrease of the interlayer separation. Certainly, it may be speculated as to whether the obvious structural tension induced by the mismatch between the tetrahedral layer and the large octahedral layer might be a crucial factor fostering the unexpected and unusual redox reactivity described in the next section.

Oxidative Cation Exchange. For further functionalization of the layered silicate toward shape/size selectivity, the interlayer space must be accessible for chemical modification. Generally, the intracrystalline reactivity of natural micas is very low. As mentioned in the Introduction, cation exchange for micas is possible in principle[12−15,43] but is slow and incomplete. Therefore, we were quite surprised by the easiness and rate of ion exchange displayed by the synthetic ferrous tainiolite. The cation exchange is complete for most crystallites as checked by EDX. Only large crystals and intergrown aggregates still contain some residual Cs^+ in the interlamellar space as seen with bulk analytical methods such as LA-ICP−MS (Table 6). Both EDX and LA-ICP−MS show a Ba content in agreement with a reduction of the interlayer charge density by roughly a factor of 2 ($Cs_{1.0} \rightarrow Ba_{0.25}$) resulting in a layer charge in the regime of smectites.

The PXRD traces for pristine and Ba^{2+}-exchanged materials are shown in Figure 3. The essential feature is the increase of the *d* value of the 001 reflection to 12.5 Å, which represents an increase of the basal spacing of the layered silicate. By comparison to the original basal spacing of 10.5 Å observed for Cs^+ as the interlayer cation, it can be reasoned that unhydrated Cs^+ was successfully replaced by Ba^{2+} now forming a monolayer hydrate[44−47] because of the higher hydration enthalpy of Ba^{2+} and/or the reduced layer charge. Additionally, this cation exchange leads to a loss of the periodic three-dimensional relationship between consecutive silicate layers represented by the decrease of the intensity of the reflections not belonging to the 00*l* series in the diffraction pattern. This is not surprising since interlayer water may act as a lubricant, fostering planar defects in the stacking direction.

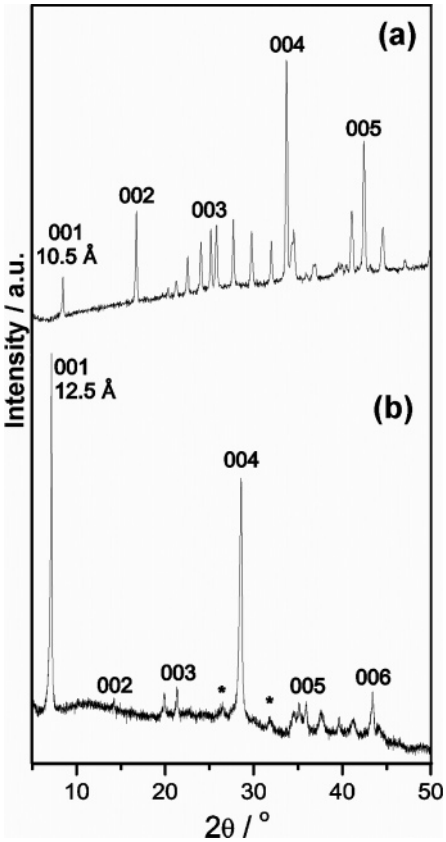

Figure 3. X-ray diffraction patterns of as-synthesized (a) and Ba^{2+}-exchanged (b) $Cs[Fe_2Li]^o[Si_4]^tO_{10}F_2$ (*: reflections of the sample holder).

Table 7. Mössbauer Parameters Obtained for Spectra Taken at 170 K of $Cs[Fe_2Li]^o[Si_4]^tO_{10}F_2$, of Ba^{2+}-Exchanged Specimen, and of Ba^{2+}-Exchanged Specimen after Aging[a]

site	IS (mm/s)	QS (mm/s)	*RA (%)*	*SR (%)*
As-Synthesized				
$[Fe^{2+}]_{M1}$	1.08	2.72	45	37
$[Fe^{2+}]_{M2}$	1.10	2.12	55	63
Ba^{2+}-Exchanged Specimen				
$[Fe^{2+}]$	1.04	2.91	23	
$[Fe^{2+}]$	1.06	2.41	44	
$[Fe^{3+}]$	0.25	0.72	12	
$[Fe^{3+}]$	0.29	0.35	21	
Ba^{2+}-Exchanged Specimen after Aging				
$[Fe^{2+}]$	1.04	2.91	24	
$[Fe^{2+}]$	1.06	2.41	28	
$[Fe^{3+}]$	0.25	0.72	27	
$[Fe^{3+}]$	0.29	0.35	21	

[a] Spectrum of $Cs[Fe_2Li]^o[Si_4]^tO_{10}F_2$ was fitted with two quadrupole doublets for Fe^{2+}; for those of the Ba^{2+}-exchanged specimen, two Fe^{3+} doublets were additionally allowed. For all doublets, a Lorentzian width of 0.25 mm/s was assumed, and an additional Gaussian broadening was allowed. For the Fe^{2+} doublets, an asymmetry caused by texture was allowed; the Fe^{3+} doublets were assumed to exhibit no texture effects. The spectra of the fresh and aged Ba-exchanged specimens were fitted simultaneously assuming that the isomer shifts and quadrupole splittings of the individual components were the same in the fresh and aged specimens. The isomer shifts are given with respect to the source of ^{57}Co in rhodium kept at 298 K. Errors of the isomer shifts and quadrupole splittings are about 0.02 mm/s; those of the relative intensities are about one percentage point. IS: Isomer shift; QS: quadrupole splitting; and RA: relative area. SR: Site occupancy determined by single-crystal refinement.

Mössbauer spectroscopy shows that upon cation exchange under aerobic conditions, a concomitant oxidation of structural Fe^{2+} has occurred. Taking into account the uncertainty

(43) von Reichenbach, H. In *Proceedings of the International Clay Conference in Madrid, 1972*; Serratosa, J. M., Ed.; Division de Ciencias, CSIC: Madrid, 1973; p 457.
(44) da Silva, G. J.; Fossum, J. O.; DiMasi, E.; Maloy, K. J. *Phys. Rev. B* **2003**, *67*, 094114.
(45) Ferrage, E.; Lanson, B.; Sakharov, B. A.; Drits, V. A. *Am. Mineral.* **2005**, *90*, 1358−1374.
(46) Ferrage, E.; Lanson, B.; Malikova, N.; Plancon, A.; Sakharov, B. A.; Drits, V. A. *Chem. Mater.* **2005**, *17*, 3499−3512.
(47) Tambach, T. J.; Bolhuis, P. G.; Smit, B. *Angew. Chem., Int. Ed.* **2004**, *43*, 2650−2652.

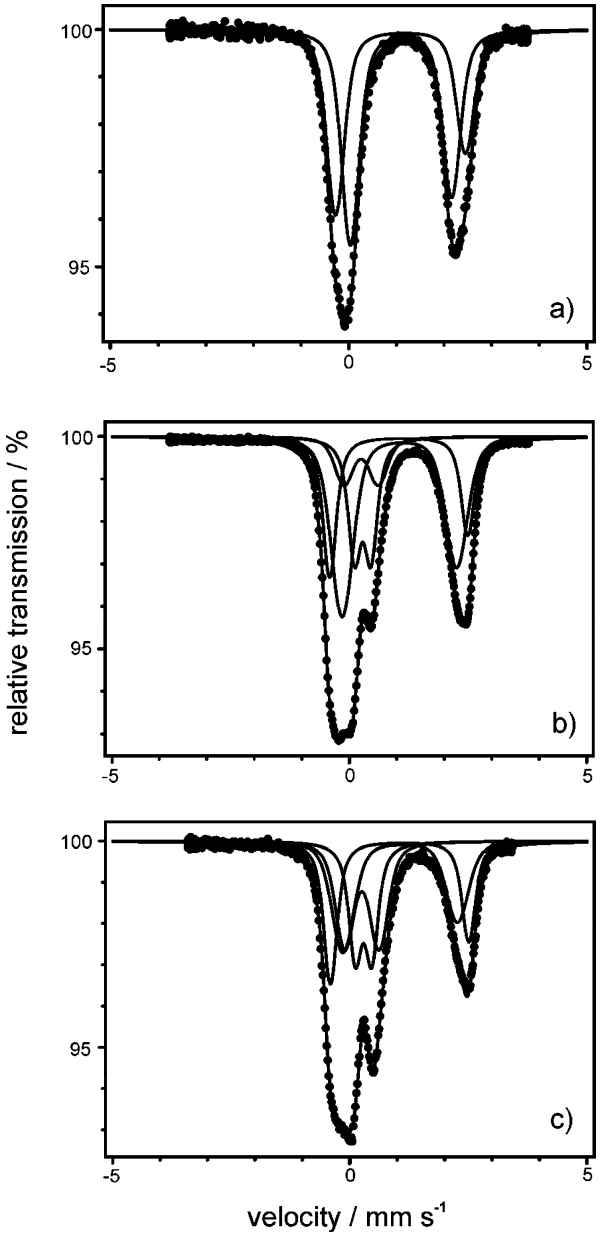

Figure 4. Mössbauer spectra of as-synthesized $Cs[Fe_2Li]^o[Si_4]^tO_{10}F_2$ (a), of Ba^{2+}-exchanged specimen (b), and of Ba^{2+}-exchanged specimen after aging (c) measured at 170 K.

of the Fe^{3+}/Fe^{2+} ratio as determined by Mössbauer spectroscopy (cf. Table 7), at a first glance, the reduction in charge density seems to correlate directly with the degree of oxidation of structural Fe^{2+}, resulting in an idealized formula of $Ba_{0.25}[Fe^{2+}_{1.5}Fe^{3+}_{0.5}Li_{1.0}]^o[Si_4]^tO_{10}F_2$. However, the reduction of the octahedral Li content as diagnosed by LA-ICP−MS (Table 6) is certainly significant and may not be neglected. It appears that the oxidation of structural Fe^{2+} not only induces a reduction in the permanent negative charge of the silicate layers but also triggers a partial transformation from a trioctahedral into a dioctahedral 2:1 layered silicate. This conclusion is further supported by a remeasurement of the Mössbauer spectrum. After 12 months of aging, the Fe^{3+}/Fe^{2+} ratio was further increased (Figure 4 and Table 7). The sample was actually never removed from the sample holder, so the total composition could not change during this continuation of oxidation. From this, it is clear that besides the removal of interlayer cations, other mechanisms for charge compensation must be active. We propose a kind of anti-Hofmann−Klemen effect,[48] where for some structural Fe^{2+} being oxidized, octahedral $[Li^+]^o$ is transferred into the interlayer space

$$[Fe^{2+}{}_2Li_1]^o \rightarrow \{Li_x\}^{int}[Fe^{2+}{}_{2-x}Fe^{3+}{}_xLi_{1-x}]^o$$

This combination of oxidation of octahedral Fe^{2+} and expelling of octahedral Li into the interlayer space will actually leave the permanent negative charge of the silicate layer unchanged. During the initial exchange in solution, interlayer Li would have been exchanged for Ba^{2+}, while during the continuation of the oxidation by oxygen from air ($O_2 + 4H^+ + 4e^- \rightarrow 2H_2O$) in the Mössbauer sample holder, it would stay in the interlamellar space. Combining the LA-ICP−MS data with Fe^{3+}/Fe^{2+} ratios as determined by Mössbauer spectroscopy (33:67, Table 7) leads to a formula that is not perfectly charge balanced ($Ba_{0.23}[Fe^{2+}_{1.34}Fe^{3+}_{0.66}Li_{0.68}]^o[Si_4]^tO_{10}F_2$). Most likely, this reflects the uncertainty in the Fe^{3+}/Fe^{2+} ratio as discussed in detail in Mössbauer Spectroscopy. Clearly, this complex redox chemistry asks for further in-depth investigations that are beyond the scope of this paper. However, it should be stressed that regardless of the details of the mechanism, this oxidative cation exchange opens a versatile and remarkable simple, hitherto unknown pathway to convert a ferrous tainiolite from a highly charged mica to a still coarse-grained but swellable smectite (hectorite).

Both hydration and reduction of the layer charge will facilitate further cation exchange into the interlayer space. Cation exchange is, of course, the key step for further functionalization of the material. With easy accessibility to the interlayer space given, further chemical modifications can be performed, leading to desired properties such as shape or size selectivity.[49] Additionally, the physical and chemical properties of the silicate layer itself can thereby be linked to the chemical system in the interlayer space. For instance, the layer charge controls the number of pillars and by this the pore size of the resulting microporous pillared clay. With ferrous hectorite, the layer charge can be adjusted easily by redox reactions, which should allow for flexible tuning of pore sizes.

Discussion of Conductivity Mechanism. For possible future applications of the investigated layered silicates, electrical conductivity is a second desirable feature besides microporosity. The electric conductivity and UV spectrum of the synthesized tainiolite $Cs[Fe_2Li]^o[Si_4]^tO_{10}F_2$ shall therefore be compared to the ones of natural biotites with the general formula $K[Mg_{3-x}Fe^{2+}{}_x]^o[AlSi_3]^tO_{10}(OH,F)_2$.

To check for any evidence of intrinsic band conductivity, UV−vis/NIR spectra of as-prepared and Ba^{2+}-exchanged $Cs[Fe_2Li]^o[Si_4]^tO_{10}F_2$ were recorded and are presented in Figure 5. Clearly, the UV spectra show no optical gap characteristic for photoconducting materials. Only weak absorption bands were observed at 8800, 10850, and 14 000 cm^{-1}, which are responsible for the brown color of the tainiolite.

(48) Hofmann, U.; Klemen, R. *Z. Anorg. Allg. Chem.* **1950**, *262*, 95−99.
(49) Breu, J.; Seidl, W.; Senker, J. *Z. Anorg. Allg. Chem.* **2004**, *630*, 80−90.

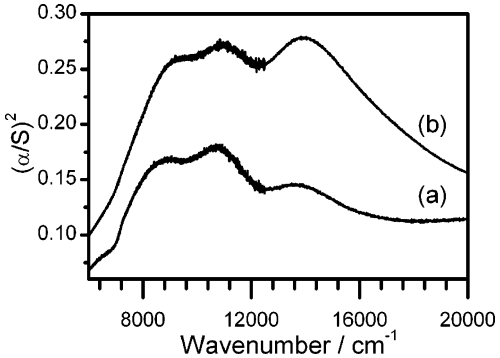

Figure 5. Transformed reflectance spectrum of as-synthesized (a) and Ba^{2+}-exchanged (b) $Cs[Fe_2Li]^o[Si_4]^tO_{10}F_2$.

The spectra of natural biotites containing iron are dominated by absorption bands near 9000, 11 000, and 14 000 cm^{-1}, which are superimposed upon a tail from a strong absorption centered in the ultraviolet region. However, the assignment of these absorption bands is discussed controversially in the literature. The two bands at 9000 and 11 000 cm^{-1} have generally been assigned to spin-allowed transitions $^5T_{2g} \rightarrow {}^5E_g$ of Fe^{2+}.[50−53] The 14 000 cm^{-1} (720 nm) band is usually assigned to a $Fe^{2+} \leftrightarrow Fe^{3+}$ interaction. Initial studies[50,51,53] associated this band with intervalence charge transfer. Later, it was suggested[54,55] that it may be caused by a magnetic interaction between pairs of Fe^{2+} and Fe^{3+} ions. Kliem and Lehmann[52] rejected these assignments and instead proposed that also the 14 000 cm^{-1} band along with the 9000 and 11 000 cm^{-1} bands are due to Fe^{2+} alone, in both the M1 and the M2 sites. The latter assignment is in contradiction to our experimental data. The comparison of almost Fe^{3+}-free as-prepared and Ba^{2+}-exchanged (partially oxidized) tainiolite shows that the intensity of the absorption band at 14 000 cm^{-1} increases with increasing Fe^{3+} content in the material. Recently, Ruscher and Gall[56,57] have observed that the main absorption feature in the spectra can be discussed using the model of small polaron absorption in disordered systems.

To our knowledge, there are no electric conductivity measurements of synthetic fluoro-micas containing transition metals. However, a few reports about electric conductivity of natural micas exist in the literature.[25−30] It is important to note that natural micas form extensive solid solutions that sometimes render the interpretation of experimental data difficult. Natural micas contain a mixture of electroactive transition metals such as Fe^{2+}, Fe^{3+}, Mn^{2+}, Mn^{3+}, Ti^{4+}, etc. in the cation sublattice. Additionally, in the anion sublattice, OH^- may be substituted by F^- or O^{2-}. The electrical conductivity of natural micas varies from 10^{-10} to 10^{-17} Ω^{-1} cm^{-1} at room temperature.[25,26]

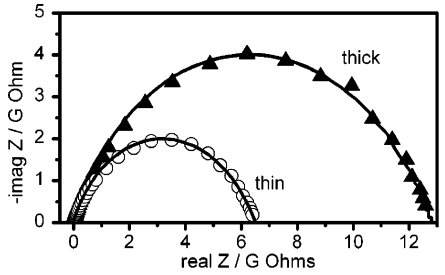

Figure 6. Complex-plane plot of the impedance at 373 K of $Cs[Fe_2Li]^o[Si_4]^tO_{10}F_2$ for two samples with different thickness: 1.05 mm (solid) and 1.65 mm (open).

A number of reports[25,27,30] has demonstrated that the electric conductivity depends on the concentration of the total iron content in mica. However, according to Meunier et al.,[27] the Fe^{3+}/Fe^{2+} ratio and Ti^{4+} content have an even stronger influence. Guseinov et al.[30] recently investigated the correlations between the chemical composition of natural micas (containing Ti^{4+} and other impurities) and the electric conductivity at 473 K. They show that the electric conductivity is mostly determined by the iron content. The conductivity increases with the rising content of Fe^{2+} according to

$$\log \sigma = -12.81 + 0.18\text{FeO (wt \% FeO)} \qquad (1)$$

and decreases with the Fe^{3+}/Fe^{2+} ratio and F^- concentration. According to the previous equation, the incorporation of two Fe^{2+} per formula unit, as in $Cs[Fe_2Li]^o[Si_4]^tO_{10}F_2$, should increase the electric conductivity by up to 5 orders of magnitude. However, the beneficial effect of increasing the Fe^{2+} content is expected to be counterbalanced to some degree by the damaging effect of fluorine on the electric conductivity of micas, which is also predicted by Hartree−Fock calculations and electron transfer theory.[58]

The frequency-dependent conductivity was measured by impedance spectroscopy. At temperatures from 333 to 450 K, the complex-plane plots consisted of single, depressed semicircles (Figure 6). The direct current (dc) conductivity was determined by extrapolation to zero frequency via a curve fit of the impedance. The equivalent circuit model consisted of a constant phase element, a resistance, and a capacitance in parallel. Above 480 K, an additional smaller semicircle appeared at low frequencies, which was subtracted in the curve fits before evaluation of the DC conductivity. The resulting DC conductivities for two samples with different thicknesses differed by less than 20%. We conclude that the measured conductivity is a bulk property with no or negligible contributions of electrode effects. Thus, we can exclude ionic conductivity because the applied gold electrodes are ionically blocking. The dc conductivity increases with increasing temperature as shown in Figure 7.

As predicted by eq 1, the electric conductivity of $Cs[Fe_2Li]^o[Si_4]^tO_{10}F_2$ at 473 K (5×10^{-9} Ω^{-1} cm^{-1}) is indeed 10^5 times higher as compared to the Fe-free congener, fluorophlogopite ($K[Mg_3]^o[AlSi_3]^tO_{10}F_2$, 10^{-15} Ω^{-1} cm^{-1}).

Several authors have used theoretical assumptions given by Schnackenberg[59] for polaron hopping conduction. We also

(50) Faye, G. H *Can. Mineral.* **1968**, *9*, 403−425.
(51) Robbins, D. W.; Strens, R. G. J. *Miner. Mag.* **1972**, *38*, 551−563.
(52) Kliem, W.; Lehmann, G. *Phys. Chem. Miner.* **1979**, *4*, 65−75.
(53) Smith, G.; Strens, R. G. J. Intervalence transfer absorption in some silicates, oxide, and phosphate minerals. In *The Physics and Chemistry of Minerals and Rocks*; Wiley: New York, 1976; pp 583−612.
(54) Smith, G. *Phys. Chem. Miner.* **1978**, *3*, 375−383.
(55) Bakhtin, A. I.; Vinokurov, V. M. *Geokhimiya* **1978**, *1*, 87−95.
(56) Ruscher, C. H.; Gall, S. *Phys. Chem. Miner.* **1995**, *22*, 468−478.
(57) Ruscher, C. H.; Gall, S. *Phys. Chem. Miner.* **1997**, *24*, 365−373.
(58) Rosso, K. M.; Ilton, E. S. *J. Chem. Phys.* **2005**, *122*, 244709.
(59) Schnakenberg, J. *Phys. Status Solidi* **1968**, *28*, 623−633.

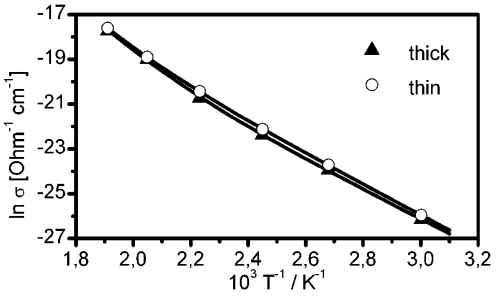

Figure 7. Temperature dependence of $Cs[Fe_2Li]^o[Si_4]^tO_{10}F_2$ for two samples with different thicknesses: 1.05 mm (solid) and 1.65 mm (open).

expect electronic hopping conduction for the present material, as evidenced by the UV−vis/NIR spectroscopy data. This model predicts a crossover from one-phonon to multiphonon processes of charge carrier hopping at $\Theta_D/2$ (Θ_D −is the Debye temperature). In the low temperature region ($T < \Theta_D/2$), the conductivity due to hopping via acoustic phonons is

$$\sigma_1 = K_1 \exp(-W_D/2kT) \quad (2)$$

In the high temperature region ($T > \Theta_D/2$), hopping occurs via polar phonons after

$$\sigma_2 = K_2 \exp(-(W_D/2 + W_H(\tan h(\Theta_D/4T))/(\Theta_D/4T))/kT) \quad (3)$$

The overall conductivity is $\sigma = s_1 + s_2$. W_D is the activation energy for acoustic phonon assisted hopping, and W_H is a function of the electron−phonon coupling constant for polar phonons.

An Arrhenius plot of the conductivity results in a slightly bended curve (Figure 7) from which we estimate $\Theta_D = 800$ K. The curve fit of the experimental data σ(T) results in $W_H = 0.50$ eV and $W_D = 1.15$ eV, with an overall activation energy of $W_H + W_D/2 = 1.07$ eV in the high temperature limit.

Currently, zeolites represent the most prominent shape- and size-selective microporous materials used as sensors. Applied as functional films in gas sensors, their selectivity can be designed to some degree by cation exchange.[60−63] It should be mentioned here that usually zeolite based chemical sensors are ionic conductors with a rather poor conductivity. These zeolites change their complex impedance[64−66] upon adsorption of analytes. Since the conductivity of zeolites is of ionic nature, only ac measurements are possible. In contrast to this, the ferrous hectorite described here provides an electronically conducting framework. Its charge carrier density is determined by the Fe^{2+}/Fe^{3+} ratio. Hence, the redox behavior of an ambient gas species (e.g., CO) might change the Fe^{2+}/Fe^{3+} ratio, resulting in a significant change in the electronic conductivity, which can be measured by a much simpler dc technique, as seen in the impedance spectrum (Figure 6). If one succeeds in preparing a microporous material by pillaring and tailoring its size and shape selectivity, a novel type of very selective gas sensors may arise.

Mössbauer Spectroscopy. Mössbauer spectra of $Cs[Fe_2Li]^o[Si_4]^tO_{10}F_2$ and of the Ba^{2+}-exchanged specimen were taken at 298 and 170 K. Expectedly, the spectra of $Cs[Fe_2Li]^o[Si_4]^tO_{10}F_2$ exhibited only Fe^{2+} quadrupole doublets. When an additional Fe^{3+} component was allowed for in the fits, its intensity turned out to be less than 3% of the spectral area. For the Ba^{2+}-exchanged specimen, on the other hand, substantial oxidation to Fe^{3+} was observed. A satisfactory reproduction of the spectral shape requires two Fe^{3+} doublets with different quadrupole splittings to be allowed. Remeasurement of the Mössbauer spectrum of the Ba-exchanged specimen after 12 months of aging in the sample holder showed that the oxidation of structural Fe^{2+} has continued in air at ambient temperature. The spectra of $Cs[Fe_2Li]^o[Si_4]^tO_{10}F_2$ and of the fresh and aged Ba-exchanged specimens are shown in Figure 4.

Although the samples were finely ground and mixed with sugar to obtain absorbers with as little texture as possible, the spectra always exhibited a pronounced asymmetry due to texture effects (Figure 4). By tilting the plane of the $Cs[Fe_2Li]^o[Si_4]^tO_{10}F_2$ absorber to an angle of 54° with respect to the direction of the γ rays, a nearly symmetrical spectrum was obtained, which demonstrates that the asymmetry is due to texture rather than to an anisotropy of the recoil-free fraction. The asymmetry of the Fe^{2+} components renders an accurate determination of the Fe^{3+} fraction in the Ba-exchanged specimen rather difficult since the Fe^{3+} pattern largely overlaps with the left components of the Fe^{2+} doublets. The separation is better at 170 K than at ambient temperature because the splitting of the Fe^{2+} doublets increases with decreasing temperature, shifting the left Fe^{2+} component toward negative velocities and hence away from the Fe^{3+} doublets. For this reason, the relative intensities of the Fe^{3+} doublets can be obtained more reliably from the 170 K spectra than from those taken at 298 K. Therefore, only the results obtained at 170 K are compiled in Table 7. The total Fe^{3+} content in the Ba^{2+}-exchanged specimen corresponds to 33% of the spectral area. Upon aging in air, the Fe^{3+} content increased considerably to 48%.

The Mössbauer spectra of $Cs[Fe_2Li]^o[Si_4]^tO_{10}F_2$ can be fitted with two components having different mean quadrupole splittings (cf. Table 7) and rather broad and overlapping Gaussian distributions of the splittings about these mean values. The variances σ of the Gaussian distributions are about 0.25 mm/s for both components, which means that one can just discern two maxima in the total distribution. It is tempting to attribute this bimodal distribution to the quadrupole patterns of iron on the M1 (trans) and M2 (cis) iron sites. The question as to which component represents the M1 and M2 sites can then be answered tentatively on the basis of the relative intensities. In the spectra, the more intense component is the one with the smaller mean quadrupole splitting. This component would then correspond

(60) Franke, M. E.; Simon, U.; Moos, R.; Knezevic, A.; Muller, R.; Plog, C. *Phys. Chem. Chem. Phys.* **2003**, *5*, 5195−5198.
(61) Moos, R.; Muller, R.; Plog, C.; Knezevic, A.; Leye, H.; Irion, E.; Braun, T.; Marquardt, K. J.; Binder, K. *Sens. Actuators, B* **2002**, *83*, 181−189.
(62) Hagen, G.; Dubbe, A.; Rettig, F.; Jerger, A.; Birkhofer, T.; Muller, R.; Plog, C.; Moos, R. *Sens. Actuators, B* **2006**, *119*, 441−448.
(63) Moos, R.; Sahner, K.; Hagen, G.; Dubbe, A. *Rare Met. Mater. Eng.* **2006**, *35*, 447−451.
(64) Dubbe, A.; Moos, R. *Electrochem. Solid-State Lett.* **2006**, *9*, 31−34.
(65) Plog, C.; Maunz, W.; Kurzweil, P.; Obermeier, E.; Scheibe, C. *Sens. Actuators, B* **1995**, *25*, 403−406.
(66) Alberti, K.; Fetting, F. *Sens. Actuators, B* **1994**, *21*, 39−50.

to the M2 sites, which occur twice as often as the M1 sites. The actual site occupancies of iron determined by the single-crystal X-ray refinement deviate somewhat from the ideal 2:1 ratio and also do not quite agree with the intensities found for the two components in the Mössbauer spectra (cf. Table 7), but this discrepancy may be attributed to an imperfect partitioning into two components by the fits of the Mössbauer spectra with two overlapping Gaussian distributions and perhaps to some extent to differences in the Lamb−Mössbauer factors for the two sites. On the other hand, it is disturbing that in the past for the M1 sites in sheet silicates a smaller splitting was inferred than for the M2 sites. In annites containing large amounts of F^- anions, for instance, Rancourt et al.[68] observed Fe^{2+} quadrupole splittings that were similar to those found in $Cs[Fe_2Li]^o[Si_4]^tO_{10}F_2$ (≈1.5 mm/s and ≈2.2 mm/s at room temperature, as compared to 1.64 and 2.41 mm/s observed in $Cs[Fe_2Li]^o[Si_4]^tO_{10}F_2$ at room temperature), but in these annites, the intensity is smaller for the doublet with the smaller splitting. Consequently, Rancourt et al.[68] attributed the smaller quadrupole splitting to the *trans*-$Fe^{2+}O_4F_2$ (M1) sites and the larger one to the *cis*-$Fe^{2+}O_4F_2$ (M2) sites. A number of Li/Fe-micas with substantial contents of F^- anions have been studied by Mössbauer spectroscopy by Gonser and Uhlig.[69] These authors also generally found larger quadrupole splittings than both the present study and that of Rancourt et al.[68] have yielded. Fitting the Fe^{2+} Mössbauer patterns with superpositions of two Lorentzian doublets, they assigned the one with the smaller splitting to the cis (M2) sites, although this is not always justified by the relative intensities they obtain. A comparison of their results with the present ones is also rendered difficult by the rather high content of other cations in their samples.

If one attributes the two mean values of quadrupole splittings found in $Cs[Fe_2Li]^o[Si_4]^tO_{10}F_2$ (Table 7) to the M1 and M2 sites, the rather wide distribution of splittings about the respective mean values can only be explained by the distribution of Fe^{2+} and Li^+ cations in the octahedrons surrounding each Fe^{2+} site. The importance of the influence of the occupancy of neighboring octahedral sites by different cations on the Fe^{2+} quadrupole splittings in sheet silicates has been pointed out, for instance, by Rancourt.[67] There is, however, no simple model by which one could relate the different possible occupancies of even the nearest neighbor cation sites by Fe^{2+} and Li^+ to electric quadrupole interactions of the central Fe^{2+} ions. Calculations of electric quadrupole interactions taking these effects into account have recently been endeavored[70,71] but are beyond the scope of the present work. A definitive explanation for the structure of the Fe^{2+} Mössbauer patterns of $Cs[Fe_2Li]^o[Si_4]^tO_{10}F_2$ can therefore not be given at present. One certainly cannot conclusively rule out that the major contribution to the overall bimodal distribution of electric quadrupole splittings is actually caused by the cation distribution, with the different ligand geometries of the M1 and M2 sites playing only a minor role.

After the Ba exchange, the Mössbauer spectra can still be fitted with two Fe^{2+} quadrupole doublets with Gaussian broadening, although with somewhat larger mean quadrupole splittings than those found in the original $Cs[Fe_2Li]^o[Si_4]^tO_{10}F_2$. In the freshly exchanged specimen, the component with the smaller quadrupole splitting is still the stronger of the two (Table 7), which supports the notion that the corresponding iron sites are those that also had the smaller splitting in the original tainiolite. To obtain satisfactory fits of the spectra, two quadrupole doublets, each with a Gaussian distribution of quadrupole splittings, must be allowed for the Fe^{3+} formed during the Ba exchange. This indicates that there are also two different sites for the ferric iron. One notes that the slow oxidation during storage in air at ambient temperature not only leaves the quadrupole splitting (QS) values of the individual components unchanged within the limits of experimental uncertainty but also leaves the intensity of the Fe^{2+} component with the larger quadrupole splitting virtually unchanged, while that of the component with the smaller splitting decreases. Concomitantly, the Fe^{3+} component with the larger splitting increases in intensity, while the one with the smaller splitting hardly changes. This shows that mainly the ferrous iron on the sites with the smaller quadrupole splitting (QS = 2.41 mm/s) oxidizes to become Fe^{3+} of the type exhibiting the larger quadrupole splitting (QS = 0.72 mm/s). The sites that this iron is occupying would thus be the ones with the more distorted electronic environment, for which one expects larger quadrupole splittings for Fe^{3+} than for the less distorted sites. On the other hand, if one follows the suggestion made earlier in this paper that a kind of anti-Hofmann−Klemen effect[48] is playing a role in the oxidation of the ferrous iron, with lithium migrating from the octahedral layer into the interlayer space, it appears reasonable to assume that this lithium stems from nearest neighbor cation sites around the iron that becomes oxidized. The Mössbauer spectra show that this is mainly iron with the smaller Fe^{2+} quadrupole splitting, and we have concluded previously that it is also the iron with the more distorted electronic environment. This supports the notion that the electronic distortion responsible for the bimodal distribution of electric quadrupole splittings is largely caused by the distribution of lithium in the neighborhood of the Mössbauer atoms.

Conclusion

The successful synthesis and characterization of $Cs[Fe_2Li]^o[Si_4]^tO_{10}F_2$ is a first step in the direction of a new interesting microporous host systems that displays sufficient conductivity due to the high content of transition metal. The successful exchange experiment opens a wide area for modifications of the material by pillaring. Together with the observed electric conductivity, this material is a promising

(67) Rancourt, D. G. *Phys. Chem. Miner.* **1994**, *21*, 250−257.
(68) Rancourt, D. G.; Ping, J. Y.; Boukili, B.; Robert, J. L. *Phys. Chem. Miner.* **1996**, *23*, 63−71.
(69) Gonser, G.; Uhlig, J. *Isotopenpraxis* **1991**, *27*, 81−86.
(70) Lougear, A.; Grodzicki, M.; Bertoldi, C.; Trautwein, A. X.; Steiner, K.; Amthauer, G. *Phys. Chem. Miner.* **2000**, *27*, 258−269.
(71) Evans, R. J.; Rancourt, D. G.; Grodzicki, M. *Am. Mineral.* **2005**, *90*, 187−195.

candidate for applications as a material for microporous chemical sensors.

Acknowledgment. We are grateful to the Deutsche Forschungsgemeinschaft (BR1408/4 and BR1408/5) and the Elitenetzwerk Bayern (International Graduate School "Structure, Reactivity, and Properties of Oxide Materials") for financial support. We thank the Bayerisches Geoinstitut, Bayreuth, for WDX and LA-ICP−MS measurements.

Supporting Information Available: Crystallographic information for $Cs[Fe_2Li]^o[Si_4]^tO_{10}F_2$. This material is available free of charge via the Internet at http://pubs.acs.org.

CM0713778